Thermo-Mechanical Modeling And Residual Stress Analysis In WEDM Of Ti-6Al-4V ELI Using Python-Based Computational Framework

Dr. Sanjay Kumar

Assistant Professor, Department of Mechanical Engineering, J.C. Bose University of Science and Technology, YMCA Faridabad-121006, Haryana, India. sanjaykpec@jcboseust.ac.in

Abstract: This study comprise of a comprehensive computational framework is developed using Python programming to simulate the residual stress distribution and phase transformation behavior in Wire Electrical Discharge Machining (WEDM) of Ti-6Al-4V ELI alloy. The proposed model integrates dynamic spark energy input, heat conduction, thermo-mechanical coupling, and phase kinetics to capture the complex interplay of thermal, metallurgical, and mechanical phenomena that define surface integrity in WEDM. A multi-physics, time-dependent approach is adopted, accounting for rapid melting and quenching cycles, latent heat effects, thermal dilation, and microstructural evolution, including martensitic (α') and ω-phase transformations. A multi-spark thermal model is employed to realistically simulate dynamic discharge behavior and predict heat deposition. The framework solves the transient heat conduction equation coupled with convective and radiative boundary conditions, phase transformation kinetics, and residual stress evolution by considering thermal stress, transformation-induced stress, plastic deformation, and volumetric strain effects. Material properties, including temperature-dependent thermal and mechanical characteristics, are incorporated into the simulation for high-fidelity modeling. The proposed computational approach provides a physics-based understanding of residual stress generation in WEDM at high, medium, and low energy levels, enabling improved control over residual stresses and microstructural properties in precision manufacturing of Ti-6Al-4V ELI components.

Keywords: Residual Stress, Python simulation, Phase transformation, Ti-6Al-4V ELI alloy, Thermo-mechanical simulation.

Nomenclature:

Symbol	Description
α	alpha hexagonal close-packed (HCP)
β	Beta phase body-centered cubic (BCC)
α'	Martensitic alpha prime phase (needle-like HCP)
α''	Martensitic alpha double-prime phase (orthorhombic)
ω	Omega phase (metastable)
ε	Emissivity (for radiation)
$\dot{\varepsilon}$	Strain rate
ν	Poisson's ratio
ρ	Density of material
σ	Stress or Stefan–Boltzmann constant (context-dependent)
∇	Gradient operator
C_p	Specific heat capacity
T	Temperature (K)
ΔT	Temperature Change

T_∞	Ambient temperature
M_s	Martensite start temperature (K)
M_ω	Critical transformation temperature for omega-phase (K)
λ	Latent heat of martensitic transformation (J/kg)
λ_ω	Latent heat of omega-phase transformation (J/kg)
γ_ω	Stabilizing/destabilizing coefficient for ω-phase
$(\partial T/\partial r)$	Radial temperature gradient
h	Heat transfer coefficient
N	Total number of sparks in a given time
P_i	Power input of each spark
$\sigma 1$	Standard deviation for heat distribution
r_i	Radial distance from the center of each spark
t	Pulse duration (s)
$Q_{WEDM}(x, y, t)$	Heat source term representing localized energy input
$Q_{phase}(T)$	Latent heat term due to phase changes
$Q_{dilation}(T, f_w)$	Thermal dilation due to phase changes
Q_{conv}	Heat loss due to Convective
Q_{Rad}	Heat loss due to radiation
$k(T)$	Thermal conductivity (W/m·K),
σ_{Resi}	Residual stress
σ_{Th}	Thermal stress
σ_{Ph}	Phase transformation stress
σ_{pl}	Plastic deformation stress
σ_{vol}	Volumetric Strain
E	Young’s modulus
$\frac{\Delta V}{V}$	Volume change due to phase transformation
$f_{\alpha'}(T)$	Martensite fraction
k	Material hardening coefficient
ε_{pl}	Plastic Strain
$f_\omega(T)$	Fraction of omega phase at temperature
γ_ω	Stabilizing/destabilizing coefficient for omega phase
$\dot{\epsilon}_{Th}$	Thermal strain rate
σ_ω	Phase transformation stress due to omega
$\dot{\epsilon}_\omega$	Thermal strain rate associated with omega transformation
k_ω	Kinetic constant for omega phase

1. Introduction

Titanium alloys are predominantly determined by the chemical composition as well as the corresponding microstructure(Wagner & Wollmann, 2013). With a density of 4.51 g/cm³, titanium is the heaviest of the light metals. At elevated temperatures, particularly above 649°C (1300°F), titanium reacts with atmospheric oxygen and nitrogen, leading to the formation of brittle interstitial compounds with carbon and hydrogen. To prevent contamination and ensure quality, reduction, melting, and other process operations should be carried out in a controlled environment. WEDM shown in Figure 1 provides a precise and efficient method for machining Ti-alloys to achieve specific surface properties. The successful application of WEDM requires a comprehensive understanding of how WEDM parameters affect the resulting surface properties.

The dielectric fluid, which is composed of hydrocarbons and polar substances like deionized water, can sometimes contaminate the surface of fatigue-sensitive components. During rapid cooling leads to the formation of martensitic structures, which alter the alloy's mechanical properties (Daniel Das et al., 2022). This cutting method can cause oxidation and other surface reactions, resulting in visible color changes that can be linked to surface chemistry and phase evolution. The diffusion kinetics of Ti-alloys in α and β phases exhibit significant differences, affecting its mechanical behavior under thermal loads. Hydrocarbon-based dielectrics can leave behind residues that compromise fatigue performance(Mishra et al., 2020).

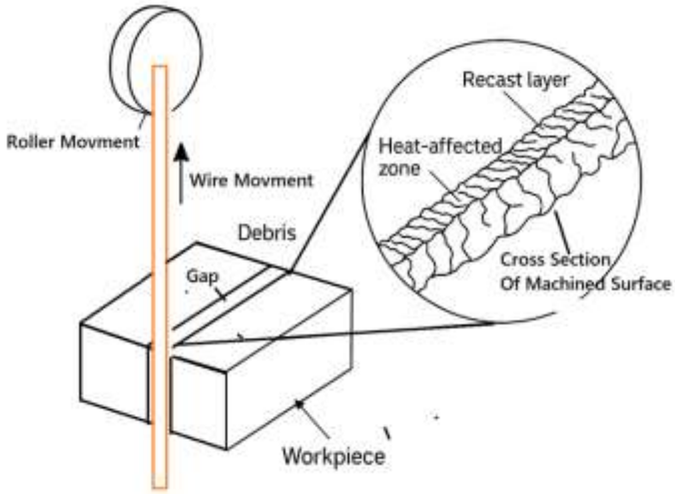

Figure 1. Schematic Wire Cut Electrical Discharge Machining Diagram

This leads to anisotropic mechanical responses due to uneven residual stresses that develop during manufacturing. To overcome these challenges and better understand the thermo-mechanical phenomena during WEDM, a physics-based computational model becomes essential. To better understand and predict these complex phenomena of cutting of Ti-6Al-4V ELI alloy, a Python-based simulation program has been proposed in this study. This program models the dynamic discharge behavior, localized heat transfer, and the resulting residual stress during WEDM. By incorporating temperature-dependent material properties, thermal gradients, and phase transformation kinetics, the simulation provides detailed insights into the evolution of surface and subsurface features. Such computational approaches not only support experimental observations but also enable the optimization of process parameters to enhance surface quality, reduce residual stresses, and improve overall machining performance.

2. Ti-6Al-4V ELI Alloy and phase transformations Overview

The Ti-6Al-4V ELI alloy is renowned for its outstanding combination of high strength-to-weight ratio and superior corrosion resistance. The "ELI" designation indicates reduced interstitial elements like oxygen, nitrogen, and carbon, which enhance its mechanical properties and ductility, especially at cryogenic temperatures. The material's low thermal conductivity characterizes its capacity to restrict heat transfer. With a low thermal conductivity of approximately 6.7 W/m·K at room temperature, the alloy acts as an effective thermal insulator. This property make it high-performance alloy that is widely used in critical applications where biocompatibility, strength, and corrosion resistance are required. A schematic β-stabilizer isomorphs phase diagram in Figure 2 illustrates a typical schematic phase diagram of titanium alloys with increasing β-stabilizer content along the X-axis. Since, the base microstructure of Ti-6Al-4V alloy primarily consists of the α-phase HCP and β-phase BCC in the α+β region at room temperature (Boyer, 2010). The diagram captures phase separation, the emergence of the ω-phase, and metastable transformations into HCP α′ or orthorhombic α″ martensite. Upon quenching from temperatures above the β-transus, the β → α′ martensitic transformation is promoted by the high cooling rates. Bignon et al., 2019 observed that after rapid cooling from above the β-transus, conventional Ti-6Al-4V predominantly forms α′ martensite, with no retained β-phase.

However, the formation of the α″ orthorhombic phase is not solely explained by rapid cooling but is influenced by the alloy's β-stabilizer concentration. Ti-alloys rich in β-stabilizers are more susceptible to forming the α″ phase (Tarín et al., 2021) (Bignon et al., 2019), though traces may also appear in conventional grades. At 600–700°C, in-situ neutron diffraction studies indicate that the intensity of α-martensite reflections increases with aging time, reflecting ongoing redistribution of V and Al between coexisting α and β phases — a phenomenon linked to α″ formation. Thermal cycling induces localized heating and cooling within material regions. During heating, inner zones can reach temperatures typical of the α+β region (e.g., between T1 and T3 in Fig. 2), causing the decomposition of α′ into equilibrium α and β phases.

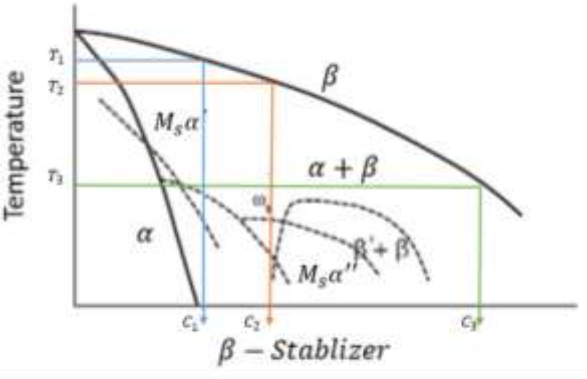

Figure 2. A schematic β-stabilizer isomorphs phase diagram showing various metastable reactions products and related phase fields(Banerjee & Williams, 2013).

Upon rapid cooling, the resulting martensitic structure depends on β-stabilizer concentration within the β-phase, At T1 (β-stabilizer content = C1), α′ martensite forms. And at T2 (β-stabilizer content = C2), a mixture of α′ and α″ martensite is observed. Whereas, at T3 (β-stabilizer content = C3), α″ orthorhombic martensite is predominantly formed. The α-β phase transformation in this alloy is extremely sensitive to temperature and cooling rates. The maximum operating temperature of titanium alloys is not primarily limited by insufficient strength, but by their relatively poor oxidation behaviour (Abd-Elaziem et al., 2024), β-phase is more susceptible than α-phase. High reactivity with oxygen and hydrogen from the ambient environment – a drawback for alloys – can cause the alloy to brittle.

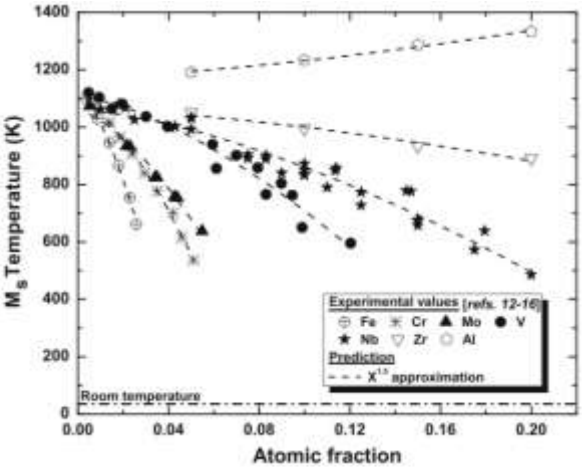

Figure 3. Concentration dependence of M_s Temperature for the Ti–X binary systems (X = Fe, Cr, Mo, V, Nb, Zr and Al) (Neelakantan et al., 2009)

The transformation into α'-martensite — a needle-like acicular structure — initiated at the martensite start temperature, depending on the concentration of β-stabilizing elements. This temperature range marks the threshold for complete β-phase stability. Precise values depend on factors including Fe, Cr, Mo, V, Nb, Ta, and W content and the alloy's thermo-mechanical processing history (Tarín et al., 2010). For Ti-6Al-4V ELI, the β-transus temperature varies between 980°C and 1010°C (Kazantseva et al., 2018). The chemical composition of alloy is presented in Table 1.

Table 1: The chemical composition of Ti-6Al-4V ELI

Element	**Titanium (Ti)**	**Aluminium (Al)**	**Vanadium (V)**	**Iron (Fe)**	**Oxygen (O)**	**Carbon (C)**	**Hydrogen (H)**
Content (wt. %)	90.0–94.0	5.5–6.8	3.5–4.5	≤ 0.25	≤ 0.13	≤ 0.08	≤ 0.015

Unlike steels, the prediction of martensite start (M_s) temperature in titanium alloys remains relatively underexplored. Upon cooling, martensite begins to form via a diffusion less, athermal transformation mechanism (Ghosh & Olson, 1994). A prominent hump observed in dilatometric curves during quenching corresponds to the formation of thermal martensite temperature. The M_s Temperature tends to decrease with increasing concentrations of alloying elements such as Fe, Cr, Mo, V, Nb, Ta, and W as shown in Figure 3. The binary predictions for M_s exhibit a smooth trend and tend to converge near the β-transus temperature of pure titanium (Ghosh & Olson, 1994). The M_s in titanium alloys can be approximated by an additive rule equation (1) across the contributing elements (Mukherjee et al., 2024; Neelakantan et al., 2009) . Whereas, Al is α-stabilizer, increases M_s, O and N interstitial elements, decrease M_s significantly (Aniołek et al., 2024).

$$M_s(°C)=950-40\ (\%V)-10\ (\%Fe)-70\ (\%O)-50\ (\%N)+30\ (\%Al) \qquad (1)$$

Depending on the alloy's chemistry, martensitic transformation results in either orthorhombic α″ or hexagonal α' structures the final $M_s(°C)$ Temperature is 951.9°C. The ω-phase also plays a pivotal role in titanium alloy transformations, especially in Ti-6Al-4V ELI. It functions both as a precursor to martensite and as a modulator of β-phase stability. Formation of ω-phase occurs through a displacive collapse of alternating β-planes, resulting in Athermal ω, forming during rapid quenching, with a complete hexagonal collapse that destabilizes β-phase and facilitates α′ nucleation or Isothermal ω, forming under slower cooling or aging, leading to a partial collapse that stabilizes the β-phase by rejecting β-stabilizers like vanadium, potentially suppressing martensite formation (Banerjee & Williams, 2013; Lütjering & Williams, 2003). The ω-phase profoundly influences the kinetics and driving forces of martensitic transformation. It increases the nucleation rate of α′ martensite and creating localized compositional gradients that either promote or hinder martensitic transformation based on thermal history and alloy chemistry (Enzinger et al., 2023). The ω-phase complete collapse accelerates α′ formation whereas Partial collapse overly stabilizes β-phase, delaying martensitic transformation (Malinov et al., 2000).

3. Simulation and computational methodology using Python programing

This study presents a Python-based computational framework simulating residual stress distribution and phase transformation behavior in Ti-6Al-4V ELI alloy during WEDM. The model combines heat conduction, spark energy input, stress-strain coupling, and phase kinetics in a dynamic thermo-mechanical simulation. WEDM involves complex interactions of thermal, metallurgical, and mechanical phenomena that influence the final surface integrity. This study aims to develop a refined thermo mechanical model that accounts for dynamic multi-spark behaviour at high, medium and low energy level. The melting and re-solidification of molten metal at surface in WEDM is very fast due to the heating and quenching of spark by surrounding dielectric during spark ‘‘OFF” off cycle at heat affected zone. The author adopts a modular, time-resolved, and physics-based approach to accurately simulate the complex phenomena. Together, these components form a comprehensive framework for understanding and controlling the thermo-physical behavior.

3.1. Phase Transformation and Thermal Dilation Kinetics:

During the spark "ON" phase**,** localized temperatures in the heated zone exceed 1500°C—well above the β-transus temperature (~995–1010°C for Ti-6Al-4V ELI) (Kazantseva et al., 2018). This rapid heating completely transforms the initial α + β microstructure into a single β-phase**.** When the spark is turned "OFF," rapid quenching occurs due to the surrounding dielectric fluid. This cooling cycle leads to solidification of the molten metal and phase transformation of the β-phase into different martensitic structures. Upon rapid heating during welding or similar thermo-mechanical processes, the β-phase begins to grow as the temperature exceeds the β-transus temperature (typically around 995°C), leading to a complete transformation of the α-phase into β-phase(Wagner & Wollmann, 2013). Recrystallization of the β-phase occurs near this temperature, refining the grain structure and boundaries. During rapid cooling (quenching), the β-phase does not have sufficient time to revert to the equilibrium α+β mixture. These complex interactions highlight the ω-phase's crucial role in controlling the microstructure and mechanical properties of Ti-6Al-4V alloys, particularly where precise phase control is essential for engineering applications. The Phase Transformation and Thermal Dilation can be represented as of latent heat during martensitic and ω-phase transformations can be expressed as (Bönisch et al., 2016; Mukherjee et al., 2024). The heat terms related to phase transformation and thermal dilation are expressed in equation (2). The phase transformation heat terms includes the latent heat released or absorbed during martensitic (α′), (ω) phase transformations. The thermal dilation heat term accounts for stress and strain rates during phase changes, given by equation (3) (Ballor et al., 2023), where thermal strain rates equation (4),(6) and phase transformation stress equation (5).

$$Q_{Phase}(T) = \lambda \frac{(df_{\alpha'})}{dT} + \gamma_\omega \lambda_\omega \frac{df_\omega}{dT} \qquad (2)$$

$$Q_{dilation}(T, f_w) = \sigma_{Ph}.\dot{\epsilon}_{Th} + \gamma_\omega \sigma_\omega \dot{\epsilon}_\omega \qquad (3)$$

Where:

$$\dot{\epsilon}_{Th} = \alpha \frac{dT}{dt} \qquad (4)$$

$$\sigma_\omega = E\frac{\Delta V}{V} f_\omega(T) \qquad (5)$$

$$\dot{\epsilon}_\omega = \alpha_\omega \frac{dT}{dt} \qquad (6)$$

In this cases, the transformation involves the ω-phase acting as an originator, an extended form considering its influence can be expressed as (Tarín et al., 2021)(Bignon et al., 2019). The martensitic α′-phase fraction evolves equation (7) the M_s and an exponential relation influenced by the ω-phase fraction equation (8) (Li & Min, 2020). Similarly, the ω-phase fraction grows with decreasing temperature below its critical transformation temperature (M_ω). Both transformations follow kinetics modeled by JMAK theory (Lekoadi et al., 2023), where the martensitic transformation rate equation (9) depends on temperature difference, material constants, and time.

$$f_{\alpha'}(T) = 1 - \exp(-k(T - M_s) - \gamma f_\omega)\, T < M_s \qquad (7)$$

$$f_\omega(T) = 1 - \exp\big(-k_\omega(T - M_\omega)\big),\ T < M_s \qquad (8)$$

$$\frac{df_{\alpha'}}{dt} = kn(M_s - T)^{n-1} \exp(-k(M_s - T)^n t) \qquad (9)$$

3.2. Multi-spark and dynamic effects thermal Model for WEDM:

A multi-spark thermal model, adapted from Shahane & Pande (2016) (Shahane & Pande, 2016) and validated experimentally by Izquierdo et al. (2012), is used to characterize discharge behavior and material removal. Each spark generates a Gaussian-distributed heat flux to model localized WEDM heat energy input and power input (P_i) of each spark as in equation (10).

$$Q_{WEDM}(x, y, t) = \sum_{i=1}^{N} \frac{P_i}{2\pi\sigma1^2} e^{-\frac{r_i^2}{2\sigma1^2}} \qquad (10)$$

The sparks are applied at intervals determined by the wire speed and pulse frequency, enabling accurate simulation of continuous heat deposition during the machining process. This dynamic discharge data drives the temperature and stress field evolution over time. The multiple spark models predict results closer to the experimental values by about 50% which is quite significant (Izquierdo et al., 2012).

$$\frac{dI(t)}{dt} = \frac{V_{Gap(t)} - I(t)R_{Dis}}{L_{Dis}} \qquad (11)$$

$$E_e = \int_0^t V_{Gap(t)}.I(t).dt = \int_0^t (R_{dis}(t)^2 + V_{Gap}(t) - I(t).R_{dis})I(t).dt \approx V_{avg}.I_p.t \qquad (12)$$

The electrical behaviour of the WEDM process is governed by the relationship between current $I(t)$, voltage $V_{Gap}(t)$, and inductance-resistance effects as in equation (11). As the energy equation incorporating dynamic Effects may be consider as in equation (12). This formulation accounts for the real-time variations in voltage and current during WEDM.

3.3. Heat Transfer Governing Equation in Discharge Gap:

In WEDM, thermal gradients refer to the temperature variations across the work piece. It is rapidly cyclic spark ON/OFF of each discharge that creates a localized high-temperature region and then rapid cooled by surrounding dielectric medium that affect. These steep temperature gradients create internal stresses that can lead to distortion, warping, and cracks. It's important to understand and control thermal gradients to avoid thermal shock or excessive thermal expansion and contraction. The transient heat conduction equation (15) represents the localized energy input from each WEDM spark, phase transformation heat, thermal dilation effects and heat losses (convection and radiation) typically modeled as a function of time and spatial position. The latent heat term accounts for the heat absorbed or released during phase transformations, such as solid-liquid transitions or martensitic transformations. The dielectric fluid removes heat via convection equation (13). The heat loss due to radiation equation (14) from exposed surfaces of the work piece as the dielectric fluid circulate only in the discharge gap the rest of the surface area remained exposed to environment set to ambient temperature (e.g., 25°C).

$$\mathrm{Q_{conv} = h(T - T_{\infty})} \qquad (13)$$

$$\mathrm{Q_{Rad}} = \varepsilon\sigma(\mathrm{T^4 - T_{\infty}^4}) \qquad (14)$$

These terms depend on temperature and are essential for accurately simulating phase changes. Finally, the velocity vector of the material (u) may also be considered in this, although in many static or quasi-static cases, this term can be neglected.

$$\rho \mathrm{C_p} \frac{\partial \mathrm{T}}{\partial \mathrm{t}} + \rho \mathrm{C_p u}.\nabla \mathrm{T} = \nabla.(\mathrm{k(T)}.\nabla \mathrm{T}) + \mathrm{Q_{WEDM}(x, y, t) + Q_{Phase}(T)}$$

$$+\mathrm{Q_{dilation}(T, f_w) - Q_{conv} - Q_{Rad}} \qquad (15)$$

3.4. Simulation framework for Residual Stress Calculation:

In this section, a simulation framework proposed to model residual stress calculation. The primary objective of this simulation is to predict the residual stress distribution along depth for High, Medium and low Power. The equation (16) for Residual stress on the WEDM-cut surface arises from the combined effects of thermal stress (equation 17), α′-phase transformation stress (equation 18), plastic deformation stress (equation 19), volumetric strain (equation 20), and stress due to ω-phase transformation. The volumetric strain contribution accounts for the volume changes associated with both martensitic and ω-phase formations. Boundary conditions in the simulation include the heat flux at the spark impact point, internal heat conduction within the workpiece, and surface cooling through convection and radiation. The initial condition assumes that the workpiece starts with a uniform temperature distribution and no pre-existing residual stress before the WEDM process. Total residual stress is:

$$\sigma_{\mathrm{Resi}} = \sigma_{\mathrm{Th}} + \sigma_{\mathrm{Ph}} + \sigma_{\mathrm{pl}} + \sigma_{\mathrm{vol}} + \sigma_{\omega} \qquad (16)$$

$$\sigma_{\mathrm{Th}} = \frac{\mathrm{E}}{1-\upsilon}\alpha\Delta\mathrm{T} \qquad (17)$$

$$\sigma_{\mathrm{Ph}} = \mathrm{E}\left(\frac{\Delta \mathrm{V}}{\mathrm{V}}\right)\mathrm{f}_{\alpha'}(\mathrm{T}) \qquad (18)$$

$$\sigma_{\mathrm{pl}} = \mathrm{k}.\varepsilon_{\mathrm{pl}} \qquad (19)$$

$$\sigma_{\mathrm{vol}} = \mathrm{E}\left(\frac{\Delta \mathrm{V}}{\mathrm{V}}\right)\mathrm{f}_{\alpha'}(\mathrm{T}) + \mathrm{f}_{\omega}(\mathrm{T}) \qquad (20)$$

3.5. Boundary and Initial Conditions:

The heat flux at the WEDM spark zone is modeled by setting the conductive heat flux equal to the localized heat input at the spark centre radius of spark $\mathrm{r = r_0}$ as in equation (21). Heat conduction within the workpiece follows the transient heat equation (22), capturing the effect of repeated spark heating. Convective and radiative cooling at the dielectric-fluid interface is imposed using the boundary condition equation (23), accounting for heat loss to the surrounding environment.

$$\mathrm{k}\left(\frac{\partial \mathrm{T}}{\partial \mathrm{r}}\right)_{\mathrm{r=r_0}} = \mathrm{Q_{WEDM}(x, y, t)} \qquad (21)$$

$$\mathrm{k}\Delta^2\mathrm{T} = \rho \mathrm{C_p}\frac{\partial \mathrm{T}}{\partial \mathrm{t}} + \mathrm{Q_{WEDM}(x, y, t)} \qquad (22)$$

$$-\mathrm{k}\left(\frac{\partial \mathrm{T}}{\partial \mathrm{r}}\right) + \mathrm{h(T - T_{fluid})} + \epsilon\sigma(\mathrm{T^4 - T_{fluid}^4} = 0 \qquad (23)$$

The initial temperature condition is set uniformly as the ambient temperature $(\mathrm{T(r, t = 0) = T_{ambient}})$ across the workpiece. This thermal boundary and initial conditions forms the basis for subsequent simulation of residual stresses through thermo-mechanical analysis of the WEDM-cut surface.

3.6. Material Properties (Ti-6Al-4V ELI) and data input in Python:

All material properties used in the simulation are considered temperature-dependent and organized into a Python dictionary for efficient access during computations. The engineering date and Material

Properties (Ti-6Al-4V ELI) include thermal conductivity etc. (Table 2) used for programing in Python and express their variation with temperature.

Table 2: Material Properties of Ti-6Al-4V ELI Alloy

Property	Symbol	Value
Density	ρ	4.43 g/cm³
Thermal Conductivity (k)	k(T)	6.60 W/m·K (20 °C) 10.6 W/m·K (315 °C) 17.5 W/m·K (650 °C)
Specific Heat Capacity	C_p	0.5263 J/g·°C
Thermal Expansion Coefficient	α	8.60 µm/m·°C
Young's Modulus	E	113.8 GPa
Poisson's Ratio	ν	0.342

The numerical model is discretized on a uniform 2D Cartesian grid ($\Delta x, \Delta y$) with time-variation based on stability criteria. The computational algorithm involves initializing material properties and mesh, applying initial conditions, applying heat fluxes, solving heat conduction, updating phase fractions, computing stresses, and post-processing results. Python libraries such as NumPy, SciPy, Matplotlib, and Numba are used. The simulation is developed using Python 3.12 within the PyCharm integrated development environment (IDE) for fast numerical computations, differential equation solving, and visualization.

3.7. Selection of Process Parameters for Controlled Power Levels in WEDM:

In this study, controllable parameters such as Pulse ON time (T_{on}), Pulse OFF time (T_{off}), Servo Voltage (V_s), and Peak Current (I_p) were selectively varied to control the discharge energy, while other parameters were kept constant to observe changes in residual stress for Ti-6Al-4V ELI (Table 3).

Table 3: WEDM Parameters for Ti-6Al-4V ELI

Parameter	Low Power Cut	Medium Power Cut	High Power Cut
Pulse ON Time	2.5 µs	5 µs	9 µs
Pulse OFF Time	24 µs	14 µs	7 µs
Peak Current	2.5 A	5 A	10 A
Servo Voltage	45 V	35 V	27 V

A zinc-coated brass wire was used with a wire feed rate of 5 mm/min and wire tension of 1000 gf. Distilled water with a dielectric pressure of 12 g/cm² was used as the coolant. The purpose of using high, medium, and low power cutting parameter settings was to maximize the material removal rate for rough cuts and finished cuts through controlled spark energy.

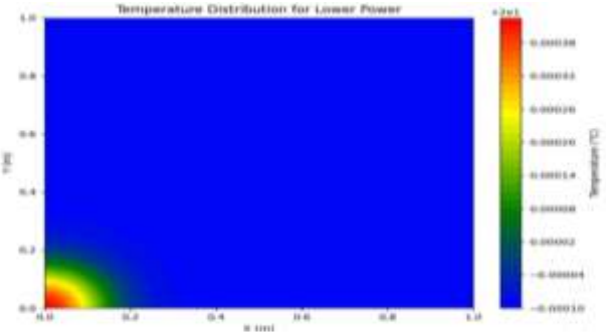

Figure 4: Temperature distribution for Low Power

This can be achieved by controlling the discharge power for each spark. The parameters sets are designed after pilot run to optimize WEDM. High power maximizes material remove rate and decrease machined surface quality by enhancing thermal distribution. To maintain a balance between material removal rate and surface roughness medium power parameters were adjusted. Low power parameters were selected to prioritize precision and minimal thermal damage of machined surface.

4. Results and Discussion

Residual stress was computed by superimposing contributions from thermal expansion mismatch, martensitic phase transformation-induced volumetric expansion, and simplified plastic deformation. The residual stress profile indicates high surface stresses decreases with depth, consistent with expected behavior in HAZ. The model captures transient heat diffusion and cooling effects over a defined.

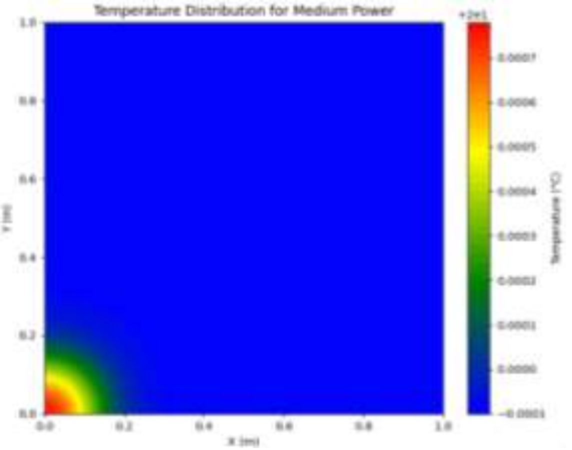

Figure 5: Temperature distribution for Medium Power

4.1. Thermal response of Ti-6Al-4V ELI under low-power :

Low power settings for WEDM are chosen to obtain high precision and superior surface finish of machined surface. The lower discharge energy produces minimal thermal gradient, yielding a very uniform temperature distribution.

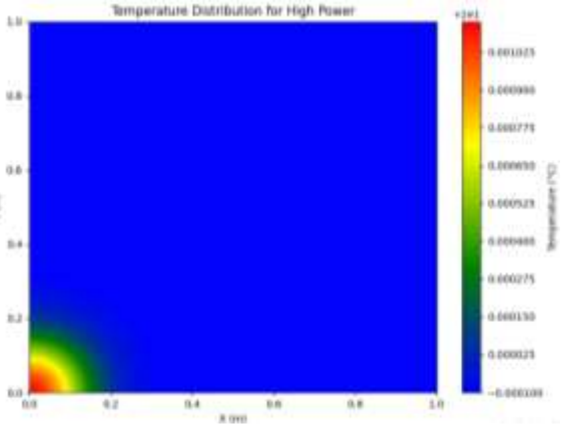

Figure 6: Temperature distribution for Medium Power

During this a slower material removal rate and this significantly reduces the risk of thermal damage. At lower discharge power, the temperature distribution still remains localized around the Heat affected Zone (HAZ), similar to other power. The maximum deviation is approximately +0.00038°C above 20°C and HAZ is smaller with the temperature gradient (Figure 4). The lower thermal gradients imply that residual stresses generated at low power are lower compared to other.

4.2. Thermal response of Ti-6Al-4V ELI under medium-power :

Simulation was conducted at a medium discharge power level for WEDM and temperature variations are extremely localized near HAZ, with maximum deviation of around +0.0007°C above 20°C . The localized spark heat input causes sharp but limited heating (Figure 5). Effective heat dissipation is observed through the workpiece surface and the dielectric medium. The extremely localized temperature rise and the sharp thermal gradients generated at surface induce significant residual stresses. Medium power serves as a balanced compromise between the extremes of high and low power operations. The discharge energy is moderated to provide a more uniform thermal profile, reducing the size and intensity of hotspots evident in the temperature plots. This allows for a controlled material removal rate while improved control over thermal effects.

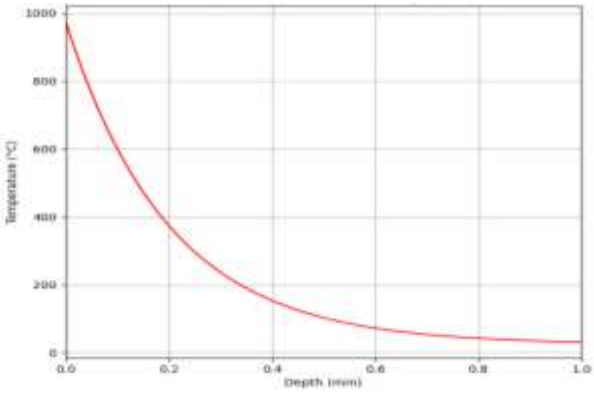

Figure 7: Temperature Distribution along Depth

4.3. Thermal response of Ti-6Al-4V ELI under High power:

At high discharge power, the temperature rise near the spark impact zone is significantly higher compared to both medium and low power conditions. The maximum temperature deviation reaches approximately +0.001025°C that is roughly 50% higher than medium power and almost three times higher than low power (Figure 6). The HAZ appears slightly larger and more intense, showing a broader spread of thermal influence. The temperature distribution plots typically display more pronounced hotspots and also indicated by larger red zone, which highlight higher localized thermal loads and residual stress.

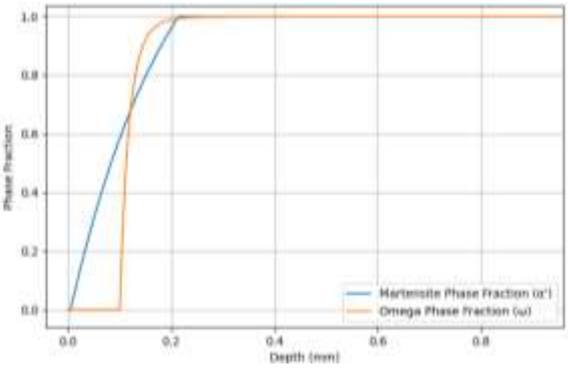

Figure 8. Phase Transformation Distribution along Depth

4.4. Temperature Distribution:

The temperature distribution (Figure 7) varies exponential decay from the surface. Peak surface temperature reaches nearly 975°C due to WEDM discharge and dielectric fluid rapidly decreasing to ambient conditions (25°C) within 0.8 mm. This distribution is similar to practical WEDM process. The exponential decrease of this temperature defines the depth of thermal and phase transformation zones along the depth from the machined surface of the Ti-6Al-4V ELI alloy. This behavior highlights that the thermal influence of the WEDM process is confined very close to the surface, emphasizing the formation of a narrow HAZ and responsible for surface residual stresses and phase transformations.

4.5. Phase Transformation Fractions:

The Figure 8 shows the variation of martensite α'-phase fraction and ω-phase fraction with depth from the Wire EDM-cut surface of Ti-6Al-4V ELI alloy. The fraction of α′-martensite was computed using an experimentally M_s temperature of 951.9°C. The transformation began strongly at the surface and tapered off around 0.6 mm depth. The ω-phase fraction calculation is based on a transformation temperature threshold of 650°C and a kinetic constant of 0.03. The ω-phase fraction was lag behind α′ in the low subsurface (0.2–0.5 mm), where moderate thermal energy favored its diffusion-controlled growth. These transformations are critical because they induce significant volumetric changes and alter mechanical response. But it is observed that martensitic transformation becomes the primary mechanism, stabilizing the microstructure at HAZ.

4.6. Residual Stress Components:

The residual stress graph (Figure 9) displays the evolution of thermal, (α′ and ω)-phase, volumetric, and plastic stresses across the depth of workpiece. It is observed that the intensity of variation is different of different stress components with WEDM-cut surface of Ti-6Al-4V ELI alloy.

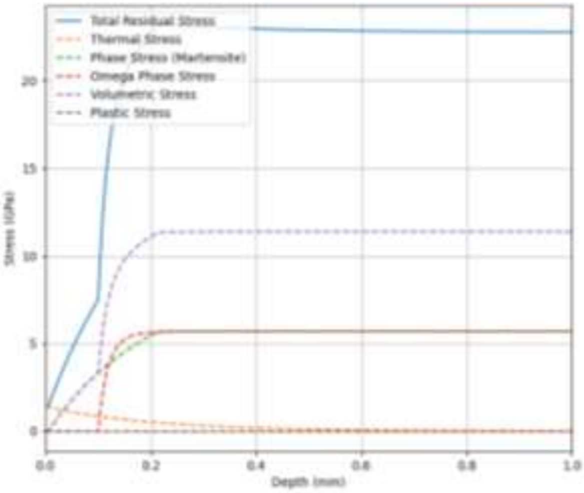

Figure 9. Residual Stress Distribution along Depth

The residual stress s near the surface is primarily influenced by volumetric, phase transformation (α′ and ω), and plastic stresses. Thermal stress is initially increases but decreases rapidly with depth, indicating the cooling effect post-spark. Volumetric stress due to phase expansion remains dominant and relatively constant beyond the near-surface region. Both (α′ and ω)-phase stresses contribute significantly near machined surface but decreased deeper into the material. Plastic stress develops near the surface due to high localized temperatures and strain, contributing to the residual stress profile. This complex stress indicates the mechanical behavior of the recast and HAZ after WEDM.

5. Conclusion

To examine the thermal, phase transformation, and residual stress behavior of Ti-6Al-4V ELI during WEDM cutting, this study developed a Python-based simulation framework. Precise high, medium, and low power conditions were established by adjusting discharge energy, pulse duration, and pulse interval, while keeping wire tension, spark voltage, dielectric pressure, wire material, and feed rate constant. The simulation showed a rapid temperature drop from ~1000 °C at the surface to near-ambient within 1 mm depth. Phase transformation analysis revealed significant α′ and ω- phase formation within the top 0.2 mm. Evaluation of residual stresses revealed that volumetric expansion, phase transformation effects, and plastic deformation dominated near-surface tensile stresses. Using Python programming enabled detailed, flexible, and accurate prediction of surface integrity outcomes. In Wire EDM-processed Ti-6Al-4V ELI, the findings show that thermal and phase transformation phenomena have a significant impact on the evolution of residual stress. These insights can be used to improve cutting parameters in precision applications. Python simulation methodology provides effective methodology in predicting surface integrity and a powerful tool for optimizing WEDM parameters in precision-critical applications such as aerospace, biomedical implants, and advanced engineering systems.

Reference

1. Abd-Elaziem, W., Darwish, M. A., Hamada, A., & Daoush, W. M. (2024). Titanium-Based alloys and composites for orthopedic implants Applications: A comprehensive review. Materials & Design, 241(March), 112850. https://doi.org/https://doi.org/10.1016/j.matdes.2024.112850
2. Aniołek, K., Barylski, A., & Rak, J. (2024). Effect of Temperature on Thermal Oxidation Behavior of Ti-6Al-4V ELI Alloy. Materials, 17(16). https://doi.org/10.3390/ma17164129
3. Ballor, J. A., Li, T., Prima, F., Boehlert, C. J., & Devaraj, A. (2023). A review of the metastable omega phase in beta titanium alloys: the phase transformation mechanisms and its effect on mechanical properties. International Materials Reviews, 68(1), 26–45. https://doi.org/10.1080/09506608.2022.2036401
4. Banerjee, D., & Williams, J. C. (2013). Perspectives on titanium science and technology. Acta Materialia, 61(3), 844–879. https://doi.org/10.1016/j.actamat.2012.10.043
5. Bignon, M., Bertrand, E., Tancret, F., & Rivera-Díaz-del-Castillo, P. E. J. (2019). Modelling martensitic transformation in titanium alloys: The influence of temperature and deformation. Materialia, 7, 100382. https://doi.org/10.1016/j.mtla.2019.100382
6. Bönisch, M., Panigrahi, A., Calin, M., Waitz, T., Zehetbauer, M., Skrotzki, W., & Eckert, J. (2016). Thermal stability and latent heat of Nb–rich martensitic Ti-Nb alloys. Journal of Alloys and Compounds, 697. https://doi.org/10.1016/j.jallcom.2016.12.108
7. Boyer, R. R. (2010). Titanium and Its Alloys: Metallurgy, Heat Treatment and Alloy Characteristics. Encyclopedia of Aerospace Engineering, December 2010, 1–12. https://doi.org/10.1002/9780470686652.eae198
8. Daniel Das, A., Sathish Kumar, K., & Prasanna, R. (2022). Investigating the effect of wire cut EDM of titanium alloy 6242 using TOPSIS. Advances in Materials and Processing Technologies, 8(3), 2824–2836. https://doi.org/10.1080/2374068X.2021.1945261
9. Enzinger, R. J., Luckabauer, M., Okamoto, N. L., Ichitsubo, T., Sprengel, W., & Würschum, R. (2023). Influence of Oxygen on the Kinetics of Omega and Alpha Phase Formation in Beta Ti–V. Metallurgical and Materials Transactions A: Physical Metallurgy and Materials Science, 54(2), 473–486. https://doi.org/10.1007/s11661-022-06881-1
10. Ghosh, G., & Olson, G. B. (1994). Kinetics of F.C.C. → B.C.C. heterogeneous martensitic nucleation-I. The critical driving force for athermal nucleation. Acta Metallurgica Et Materialia, 42(10), 3361–3370. https://doi.org/10.1016/0956-7151(94)90468-5
11. Izquierdo, B., Plaza, S., Sánchez, J. A., Pombo, I., & Ortega, N. (2012). Numerical prediction of heat affected layer in the EDM of aeronautical alloys. Applied Surface Science, 259, 780–790. https://doi.org/10.1016/j.apsusc.2012.07.124
12. Kazantseva, N., Krakhmalev, P., Thuvander, M., Yadroitsev, I., Vinogradova, N., & Ezhov, I. (2018). Martensitic transformations in Ti-6Al-4V (ELI) alloy manufactured by 3D Printing. Materials Characterization, 146(September), 101–112. https://doi.org/10.1016/j.matchar.2018.09.042
13. Lekoadi, P. M., Tlotleng, M., Siyasiya, C. W., & Masina, B. N. (2023). Investigation of network microstructure of TiB/Ti6Al4V-ELI composite manufactured with laser metal deposition. MRS Advances, 8(10), 602–606. https://doi.org/10.1557/s43580-023-00576-4
14. Li, M., & Min, X. (2020). Origin of ω-phase formation in metastable β-type Ti-Mo alloys: cluster structure and stacking fault. Scientific Reports, 10(1), 1–15. https://doi.org/10.1038/s41598-020-65254-z
15. Lütjering, G., & Williams, J. C. (2003). Titanium. Springer. https://books.google.co.in/books?id=GwI9ul_wAegC
16. Malinov, S., Sha, W., & Guo, Z. (2000). Application of artificial neural network for prediction of time-temperature-transformation diagrams in titanium alloys. Materials Science and Engineering: A, 283(1–2), 1–10. https://doi.org/10.1016/S0921-5093(00)00746-2
17. Mishra, R. R., Kumar, R., Sahoo, A. K., & Panda, A. (2020). Machinability behaviour of biocompatible Ti-6Al-4V ELI titanium alloy under flood cooling environment. Materials Today: Proceedings, 23, 536–540. https://doi.org/https://doi.org/10.1016/j.matpr.2019.05.402
18. Mukherjee, S., Basu, J., & Mandal, R. K. (2024). Structural transformations and characterisation in nano-engineered alloys. Progress in Crystal Growth and Characterization of Materials, 70(1), 100606. https://doi.org/10.1016/j.pcrysgrow.2023.100606
19. Neelakantan, S., Rivera-Díaz-del-Castillo, P. E. J., & van der Zwaag, S. (2009). Prediction of the martensite start temperature for β titanium alloys as a function of composition. Scripta Materialia, 60(8), 611–614. https://doi.org/10.1016/j.scriptamat.2008.12.034
20. Shahane, S., & Pande, S. S. (2016). Development of a Thermo-Physical Model for Multi-spark Wire EDM Process. Procedia Manufacturing, 5, 205–219. https://doi.org/10.1016/j.promfg.2016.08.019
21. Tarín, P., Gualo, A., Simón, A. G., Piris, N. M., & Badía, J. M. (2010). Study of alpha-beta transformation

in Ti-6Al-4V-ELI. Mechanical and microstructural characteristics. Materials Science Forum, 638–642, 712–717. https://doi.org/10.4028/www.scientific.net/MSF.638-642.712

22. Tarín, P., Gualo, A., Simón, A. G., Piris, N. M., Badía, J. M., Aniołek, K., Barylski, A., Rak, J., Boyer, R. R., Gangireddy, S., Mates, S. P., Bignon, M., Bertrand, E., Rivera-Díaz-del-Castillo, P. E. J., Tancret, F., Blenkinsop, P. A., Ahmed, T., Rack, H. J., Spectrometry, F., … Muraca R. F., W. J. S. (2021). Martensite formation in titanium alloys: Crystallographic and compositional effects. Materials Science and Engineering A, 872(4), 159636. https://doi.org/10.1016/j.jallcom.2021.159636
23. Wagner, L., & Wollmann, M. (2013). Titanium and Titanium Alloys. In Structural Materials and Processes in Transportation. https://doi.org/10.1002/9783527649846.ch4